PAPER

Low-temperature solution synthesis of CuO/Cu₂O nanostructures for enhanced photocatalytic activity with added H₂O₂: synergistic effect and mechanism insight†

Xiaolong Deng, Chenggang Wang, Minghui Shao, Xijin Xu* and Jinzhao Huang*

Cu$_x$O (CuO, CuO/Cu$_2$O, and Cu$_2$O) nanostructures have been controllably synthesized through a facile low-temperature solution method. The morphologies and compositions of Cu$_x$O nanostructures were well controlled by tuning the reductant amount of hydroxylamine hydrochloride, which experienced the transformation of nanosheets to octahedrons as well as the phase change of CuO to Cu$_2$O. The as-grown samples showed photodegradation selectivity to MO (maximum photocatalytic efficiency of 52% for methyl orange (MO) and 16% for rhodamine B (RhB) after 180 min photodegradation) and different photocatalytic activities in the absence or presence of H$_2$O$_2$ (62% without H$_2$O$_2$ and 82% with H$_2$O$_2$). The morphological transformations of as-grown samples were observed after the photocatalytic measurement in the presence of H$_2$O$_2$. The structural and morphological features after photodegradation were studied by XPS, SEM, and TEM investigations, revealing the possible mechanism of the as-prepared samples whereby the photodegradation of organic dyes occurred on the surface with respect to the adsorption ability, structure, and morphology of Cu$_x$O. In addition, H$_2$O$_2$ played an important role in the photodegradation of organic dyes.

1. Introduction

Environmental pollution induced by the remarkable developments of industry, especially wastewater generated by organic dye pollutants, has become one of the most detrimental issues for the sustainable development of human beings.[1–4] Therefore, it is very meaningful to explore efficient photocatalysts for environmental applications such as wastewater treatment.[5,6] In view of visible light covering the main band of solar light, the photocatalysts driven by visible light generate highly efficient photocatalytic activity due to the better utilization of available solar irradiation ($\lambda \geq 400$ nm).[6–8] Among them, photocatalysts with a narrow bandgap have attracted considerable attention due to the abilities of these photocatalysts to sufficiently utilize the available solar irradiation ($\lambda \geq 400$ nm).[6–8] Herein, discovering new photocatalytic materials with small bandgaps is an important way to adsorb the full-spectrum of visible light, in addition to modifying large bandgap photocatalysts by doping or constructing heterojunctions.[9,10] Many efforts have been made to seek and fabricate narrow bandgap materials, such as g-C$_3$N$_4$,[11,12] Sn$_3$O$_4$,[13] Ag$_2$S,[14] α-Fe$_2$O$_3$,[15] BiVO$_4$,[16] CuO,[17] Cu$_2$O,[3,18] *etc.* Among them, Cu$_x$O ($x = 1$, 2), as the typical narrow bandgap material, have attracted

School of Physics and Technology, University of Jinan, 336 Nanxin Zhuang West Road, Jinan, Shandong Province, 250022, People's Republic of China. E-mail: sps_xuxj@ujn.edu.cn; ss_huangjinzhao@ujn.edu.cn

† Electronic supplementary information (ESI) available. See DOI: 10.1039/c6ra27634b

tremendous interest for their great potential due to their unique optical and charge transport properties.[6,19–23] In addition, copper oxides (CuO and Cu$_2$O), as p-type semiconductors, are available to absorb visible light due to their favorable bandgaps of 1.3–2.1 eV for CuO and 2.1–2.6 eV for Cu$_2$O.[6,18,23]

Cu$_2$O, as one of the low-cost, non-toxicity, and abundant reserve metal oxides, has been firstly demonstrated promising photocatalytic activity for water splitting under visible light irradiation in 1998.[24] Since then, many efforts have been made to study the photocatalytic properties of Cu$_2$O by tuning their morphologies, sizes, compositions, and architectures.[3,18,25–30] Ganguli *et al.*[3] reported the morphology-dependent photocatalytic activities of nanocrystalline Cu$_2$O and they found that the layered Cu$_2$O showed the highest photocatalytic activity. Knecht *et al.*[18] revealed that the photocatalytic activity of as-prepared Cu$_2$O was controlled by the charge of the inorganic interface, the composition of the materials, and the surface area of the catalytic structures. Zhong *et al.*[27] explored the effects of various structures on the photocatalytic performance of Cu$_2$O, and they found that the hierarchical structure displayed the best result in photodegradation compared with nanoscale and microscale structures. Besides, CuO also showed the excellent properties on the promising applications, such as gas sensors,[31,32] CO oxidation catalysts,[33] lithium-ion batteries,[19,34] supercapacitor,[35] photocatalysts in H$_2$ production[36] and so on. The factors affecting the photocatalytic properties of CuO on organic pollutants were widely investigated. Zaman *et al.*[37] synthesized

petals and flowers like CuO, for which the structures played a significant role in the photodegradation of organic dyes. The size effect of CuO on the photocatalytic activity was also investigated by Wang et al.,[38] which confirmed that the as-prepared sheet-like nanostructures exhibited enhanced photocatalytic activity. In a word, the physical and chemical properties of Cu_2O and CuO were significantly influenced by their structures, morphologies, sizes and so on.[39–41]

In addition, the formation of CuO/Cu_2O composites and $CuO–Cu_2O$ mutual transformation and the related properties have also been investigated. For example, CuO hollow nanostructures were transformed from Cu_2O nanocubes by a controlled oxidation reaction using aqueous ammonia solutions and presented excellent electrochemical performance.[19] Chen et al.[21] fabricated CuO/Cu_2O composite hollow polyhedrons by thermal decomposition from metal–organic framework templates, exhibiting excellent cycle performance as anodes for lithium-ion battery. Knecht et al.[18] investigated the correlation between surface structure and photocatalytic functionality of Cu_2O/CuO composites synthesized via a synthetic solution method by tuning the ratio and concentration of Cu^{2+} and glucose. Scuderi et al.[42] synthesized CuO nanowires by a thermal process and followed by transforming to Cu_2O with subsequent thermal annealing, exploring the polycrystalline structure dependent photocatalytic activity. Meanwhile, Banerjee et al.[43] reported the fabrication of $CuO@Cu_2O$ core–shell nanowires by the carbothermal reduction method with controlled temperature and reaction time, revealing the indirect phase transformation on the surface. Stimulated by the excellent properties and their potential applications, tremendous attention had been paid to synthesize Cu_xO (Cu_2O and CuO) materials with different morphologies.[42–47] However, these methods require high temperature, complicated process, or long reaction times. Therefore, it is very interesting and important to develop a sustainable, facile, and low-temperature approach to fabricate Cu_xO materials with controlled morphologies and compositions and systematically investigate the effect of morphology and composite on the photocatalytic activity.

In this work, a facile solution method was demonstrated to controllably grow Cu_xO nanomaterials under low temperature. The structures and morphologies of as-prepared Cu_xO samples were systematically investigated by tuning the amount of hydroxylamine hydrochloride. The photocatalytic activities of Cu_xO samples for methyl orange (MO) and rhodamine B (RhB) were performed with or without H_2O_2. The post-photodegradation analysis was carried out to explore the possible mechanism for the evolution of photocatalytic activity under different conditions.

2. Experimental

2.1 Synthesis of Cu_xO nanostructures

All the chemical reagents, such as copper(II) nitrate trihydrate ($Cu(NO_3)_2 \cdot 3H_2O$), hexamethylene tetramine (HMTA), sodium hydroxide (NaOH), and hydroxylamine hydrochloride (NH_2-OH·HCl), purchased from Sinopharm Chemical Reagent Co., Ltd. (SCRC, China), were of analytical grade and used without further purification. A typical process was used as follows:

5 mmol $Cu(NO_3)_2 \cdot 3H_2O$ (1.208 g) and 2.5 mmol hexamethylene tetramine (HMTA) (0.3523 g) were dissolved into 50 mL deionized water with vigorous magnetic stirring, respectively. Then, the two solutions were mixed together followed by magnetic stirring for 10 min to form a homogeneous solution. After that, the mixture added with 9 mL NaOH (2.0 M) was immediately transferred into the water bath at 80 °C for 30 min with magnetically stirring. Subsequently, different amount of 0.4 M hydroxylamine hydrochloride was injected into the above solution quickly and kept at 80 °C for another 30 min. Thereafter, the reactor was taken out to cool down to room temperature naturally after finishing the reaction. The precipitants were collected by centrifugation and washed with ethanol and distilled water for several times. Finally, the products were obtained by drying the precipitates at 60 °C for 12 hours in a vacuum oven. The samples were named as V0, V2.5, V5, V7.5, and V10 for the hydroxylamine hydrochloride amounts of 0, 2.5, 5, 7.5, and 10 mL, respectively.

2.2 Characterization

X-ray powder diffraction (XRD) patterns of as-prepared samples were conducted on a German X-ray diffractometer (D8-Advance, Bruker AXS, Inc., Madison, WI, USA) equipped with Cu K_α radiation ($\lambda = 0.15406$ nm). The morphologies of as-prepared samples were observed by a field emission scanning electron microscope (FESEM, FEI Quanta FEG250, FEI, Hillsboro, USA) and transmission electron microscope (TEM, HEOL-200CX, JEOL, Tokyo, Japan). The X-ray photoelectron spectroscopy (XPS) was collected on the Thermo ESCALAB 250XI electron spectrometer equipped with Al Kα X-ray radiation ($h\nu = 1486.6$ eV) as the source for excitation. The Brunauer–Emmett–Teller (BET) specific surface areas of as-prepared samples were measured by N_2 adsorption–desorption isotherm with a Quantachrome NOVAtouch LX4 apparatus.

2.3 Photocatalytic properties

The photocatalytic properties were characterized by a UV-vis spectrophotometer (TU-1901, Beijing Purkinje General Instrument Co., Ltd, Beijing, China) at room temperature in air under visible-light irradiation, which was similar to previous reports.[46] The visible light was generated by a 500 W Xe lamp equipped with a cutoff filter ($\lambda \geq 420$ nm) to remove the UV part. Typically, 30 mg of the as-prepared samples were placed into 50 mL of 5 mg L^{-1} rhodamine (RhB) or 20 mg L^{-1} methyl orange (MO) aqueous solution. The mixture was moved into the photocatalytic reactor and kept in the dark for 60 min with magnetic stirring to reach the adsorption–desorption equilibrium of RhB or MO on the surface of as-synthesized Cu_2O/CuO samples. A certain amount (0 or 1000 μL) of H_2O_2 was added into the solution before turning on Xe lamp. ca. 3 mL suspension was taken out after a given irradiation time interval and centrifuged to filtrate the sample powders for the UV-vis spectra test. The concentration of RhB in the solution was evaluated by collecting the absorbance of RhB at 553 nm or MO at 464 nm from the absorption spectrum recorded by UV-vis spectrophotometer.
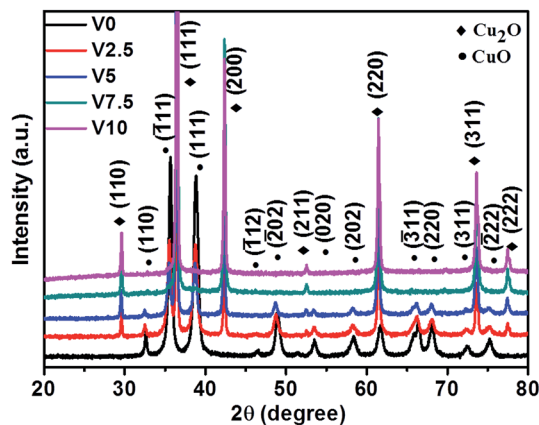
Fig. 1 XRD patterns of as-prepared Cu$_x$O samples with various amounts of hydroxylamine hydrochloride (V0-0 mL, V2.5-2.5 mL, V5-5 mL, V7.5-7.5 mL, and V10-10 mL).

3. Results and discussion

3.1 Structural and morphological characterization of samples

The XRD patterns in Fig. 1 show that all the peaks can be perfectly indexed into cubic Cu$_2$O (JCPDS no. 78-2076) and monoclinic CuO (JCPDS no. 89-5899). No other characteristic peaks are found in theses samples, which demonstrate the purity of as-synthesized samples. With the increase of hydroxylamine hydrochloride content, the compositions change from pure CuO (V0) into mixed CuO/Cu$_2$O (V2.5 and V5), finally obtaining pure Cu$_2$O (V7.5 and V10). After the amount of hydroxylamine hydrochloride reaches to 7.5 mL, there is no

influence on the composition of as-prepared samples. In a word, the results confirm that the amount of hydroxylamine hydrochloride has significant influence on the compositions of as-prepared samples.

Fig. 2a shows that the pure CuO (V0) was completely composed of nanosheets. With the increase of the amount of hydroxylamine hydrochloride to be 2.5 mL, the sample (V2.5) mainly consisted of nanosheets accompanying with some octahedral-like crystals as depicted in Fig. 2b. From the magnified SEM image (Fig. 2c), we can observe that the octahedron-like structures were perfectly formed by the assembly of nanosheets. As further increasing the amount of hydroxylamine hydrochloride to 5 mL, the octahedral-like structures became the dominant morphology in the sample (V5), as shown in Fig. 2d, though the nanosheets still existed on the surface of octahedrons from the inset of Fig. 2d. In other word, the nanosheets were almost entirely assembled to form octahedrons. With further increasing the amount of hydroxylamine hydrochloride reductant, the octahedrons as the dominant morphology were observed with non-uniform sizes as shown in Fig. 2e as well as some of truncated octahedrons for samples V7.5. From high magnification image (inset in Fig. 2e), the octahedral surfaces were rough, which was different from the smooth surfaces of octahedrons of V10 as depicted in Fig. 2f. In addition, only the octahedrons were observed with non-uniform sizes in sample V10. Combining with XRD results, the morphology transformed from the nanosheets into octahedrons by the self-assembly with the help of hydroxylamine hydrochloride.

Fig. 3 presents the typical TEM images and corresponding SAED patterns of the representative as-synthesized products V2.5 and V10. The main morphology of nanosheets was
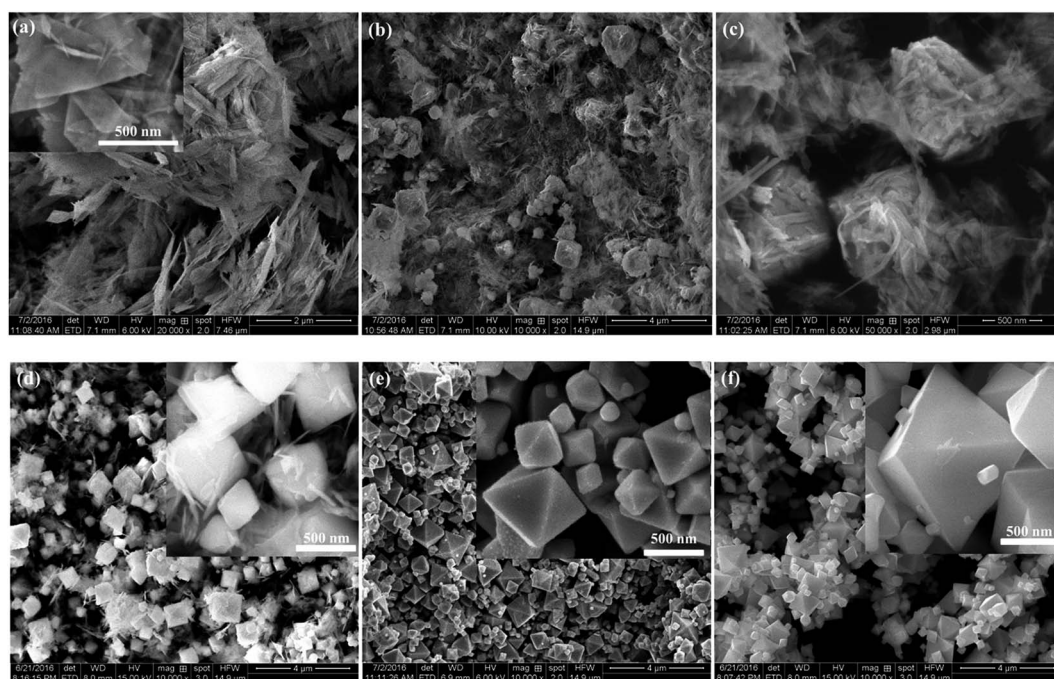

Fig. 2   SEM images of the as-synthesized samples with different amount of hydroxylamine hydrochloride during the preparing process: (a) V0, (b and c) V2.5, (d) V5, (e) V7.5, and (f) V10.

depicted as shown in Fig. 3a and b, which was consistent with SEM observation. The corresponding SAED pattern (Fig. 3c) confirmed the co-existence of CuO and Cu_2O in agreement with XRD results. However, the particles were only observed for sample V10 as exhibited in Fig. 3d–f, and the related SAED illustrated the pure polycrystalline Cu_2O, in keeping with the results of SEM and XRD.

The growth mechanism for the formation of CuO nanosheets was predicted, where HMTA played an important role in the growth process. The related chemical reactions were listed as follows according to the previous reports:[45,48,49]

$$C_6H_{12}N_4 + 6H_2O \rightarrow 6HCHO + 4NH_3$$

$$NH_3 + H_2O \rightarrow NH_4^+ + OH^-$$

$$Cu^{2+} + 2OH^- \rightarrow Cu(OH)_2$$
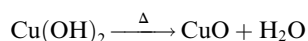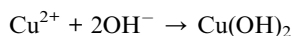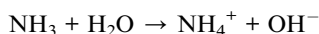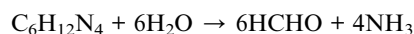
$$Cu(OH)_2 \xrightarrow{\Delta} CuO + H_2O$$

HMTA could be hydrolyzed in the solution and generate OH^- ions slowly by decomposing into formaldehyde (HCHO) and ammonia (NH_3). Then, $Cu(OH)_2$ could be formed by the chemical reaction of Cu^{2+} with OH^- ions. At the same time, HMTA acted as a surfactant which could control the nanostructure shapes.[45,50] After adding NaOH, the formation of $Cu(OH)_2$ became quickly, which could be confirmed by the color evolution of solutions (see ESI Fig. SI-1†). In brief, the transparent solution was changed

into a little lightly blue turbidity by mixing the solutions of $Cu(NO_3)_2 \cdot 3H_2O$ and HMTA together. After the addition of NaOH the color changed into blue immediately due to the instant dissolution of NaOH into OH^- ions, which confirmed the fast formation of $Cu(OH)_2$ nuclei. Then the solution was changed into dark by heating in the water bath, demonstrating the formation of CuO by the decomposition of $Cu(OH)_2$. Therefore, the nanosheets structure of CuO was controlled by HMTA in our work, which was consistent with previous report.[45,49] This was also verified by replacing HMTA with sodium dodecyl sulfate (SDS) to generate flower-like morphology consisting of nanorods, as shown in Fig. SI-2,† where XRD pattern certifying the formation of pure CuO phase. NaOH made the nanosheets aggregate together rather than individual structures due to its strong electrolyte neutralizing the surface charges of CuO.[45] However, once hydroxylamine hydrochloride was added into the above solution, the solution changed into yellow color, which intuitively demonstrated the successful transformation of CuO to Cu_2O, according to the following chemical reaction:[45,51–53]

$$2CuO + 2NH_2OH \cdot HCl \rightarrow Cu_2O + N_2 + 2HCl + 3H_2O$$
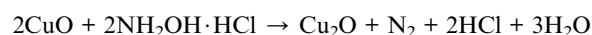
Hydroxylamine hydrochloride provides two things in the growth process: first, it would reduce Cu^{2+} ions to Cu^+ ions resulting in the formation of Cu_2O.[54] Second, it could offer binding sites to adsorb copper ions,[55,56] affected the different growth rate along [100] and [111] direction, resulting in the final shape of the products.[53] The formation of truncated octahedrons and pure octahedrons was ascribed to the following
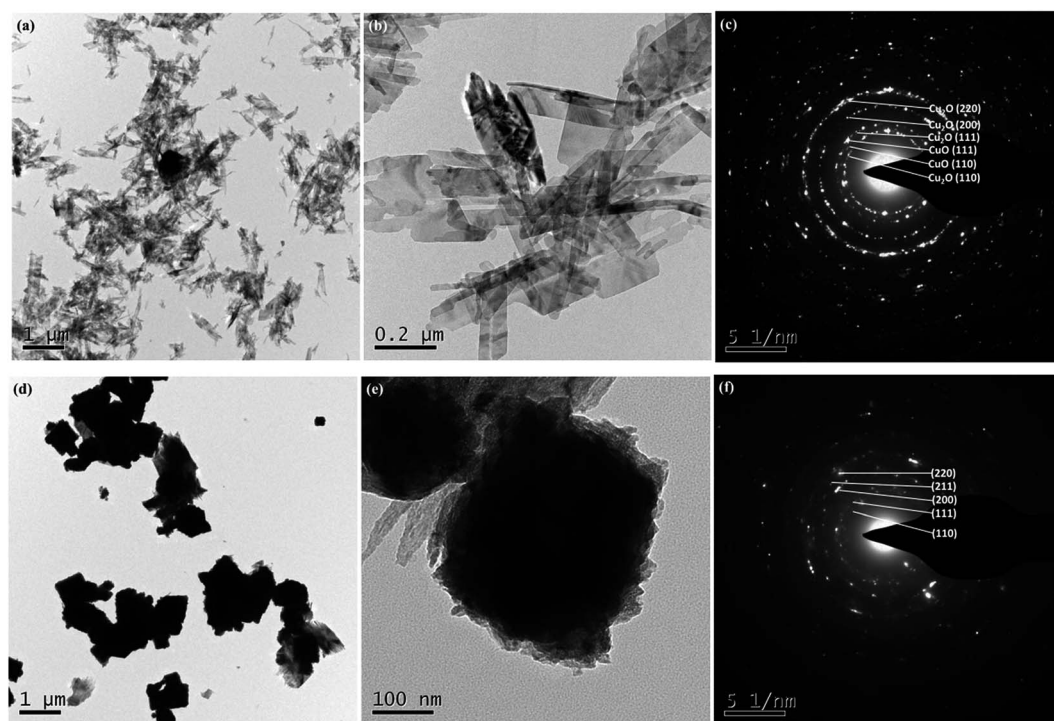

Fig. 3 Typical low and high magnification TEM images of the as-prepared products and their corresponding SAED patterns: (a−c) V2.5 and (d−f) V10.

reasons, in accordance with previous reports:[49–53] (1) HMTA preferentially adsorbing on the (111) planes of Cu_2O impeded the growth of (111) planes; (2) the amount of hydroxylamine hydrochloride may affect the growth rate along the [100] direction relative to that of the [111] direction resulting in the preferential orientation in [111] direction, which is mainly responsible for the shape control of as-synthesized samples; (3) the generated nitrogen gas influences the surface of the as-synthesized samples, such as rough surfaces; (4) the aggregated flower-like CuO nanosheets also provides the favorable conditions to form the octahedral structures.

3.2 Photocatalytic activity of as-grown samples

The photocatalytic properties of as-obtained samples were investigated (UV-vis spectral variations of RhB and MO in aqueous solution were shown in ESI: Fig. SI-3 and SI-4,† respectively) and the selective photodegradation property was performed, as shown in Fig. 4. The as-prepared samples present different photocatalytic activities to MO and RhB. V0 and V2.5 show more efficient photodegradation to RhB, while V5, V7.5 and V10 exhibit excellent photocatalytic activities to MO. The difference could be ascribed to the preferred adsorption ability of Cu_2O to anionic MO[57] and CuO to RhB,[58] respectively. Therefore, the well adsorbed dyes on the surfaces of samples promoted the photocatalytic activities. As aforementioned XRD results, CuO phase in the samples gradually decreases until disappeared with the increase of hydroxylamine hydrochloride amount, resulting in the degressive photodegradation ability to RhB, as depicted in Fig. 4a. However, the photocatalytic activities enhanced accompanying with the phase transformation from CuO to Cu_2O in Fig. 4b. In addition, Cu_2O shows the higher photocatalytic activity than CuO for MO degradation, which is consistent with previous reports.[18,57–59] Fig. 4c depicts the cycling test of as-prepared samples for MO photodegradation under visible light irradiation and illustrates the moderate recycling ability as photocatalysts for photodegradation of MO in aqueous solution except for the first run especially for sample V10. This could be caused by the photocorrosion of Cu_2O to form CuO due to Cu^+ scavenging holes at the first run,[18,46,60,61] then, the generated CuO could protect the surface of Cu_2O to inhibit the photocorrosion.[6] Moreover, all the samples exhibit relatively low efficiency to MO and RhB photodegradation.

As we know that H_2O_2 played an important role in the photocatalytic process of Cu_xO catalysts.[6,29,47,62] Hence, H_2O_2 was used in this work to improve the photocatalytic activity of as-grown samples for MO (UV-vis spectra of MO aqueous solution in the presence of H_2O_2 and as-prepared catalysts were shown in ESI: Fig. SI-5†). Fig. 5a presents the photodegradation analysis of MO in the presence of H_2O_2 under visible light irradiation. The concentration of MO in the solution is almost no change in the presence of H_2O_2 and visible light illumination illustrating the very weak activity of H_2O_2 for MO photodegradation in consistent with previous report.[62] In the presence of both H_2O_2 and catalysts under visible light illumination, the concentrations of MO in the solution were decreased promptly. The photocatalytic degradation kinetics of MO aqueous solution was analyzed by the pseudo first-order model to determinate the rate constant of photodegradation with respect to the degradation time by the following equation:[3,37,46]

$$\ln(C/C_0) = -kt$$

where C_0 is the initial concentration of MO, C is the concentration at time t, and k is the reaction rate constant. The rate constant (k) were given by the slopes of linear fit and estimated to be 0.0025, 0.0033, 0.0043, 0.0045, and 0.0056 min^{-1} for sample V10, V7.5, V0, V5, and V2.5, respectively, which were higher than other reports such as micro-nano hierarchical Cu_2O,[27] Cu_xO nanorod arrays,[6] CuO and Cu_2O nanowires,[42] although this comparison could be very difficult due to the wide range of experimental conditions used in the literature.[42] The result demonstrates that the photocatalytic performance of the samples follows the order: V2.5 > V5 > V0 > V7.5 > V10, which is different from the order in the absence of H_2O_2 as shown in Fig. SI-6† (V10 > V7.5 > V5 > V2.5 > V0). In order to study the durability of as-prepared samples, the cycle runs in the photodegradation of MO aqueous solution in the presence of H_2O_2 and catalysts under visible light irradiation are carried out in the same conditions, as presented in Fig. 5c. The observed results have no significant difference after 3 cycles, indicating the as-grown samples exhibit relatively good durability as photocatalysts for photodegradation of MO in aqueous solution.

Based on the above results, the photocatalytic mechanism could be proposed as follows combining with the reported
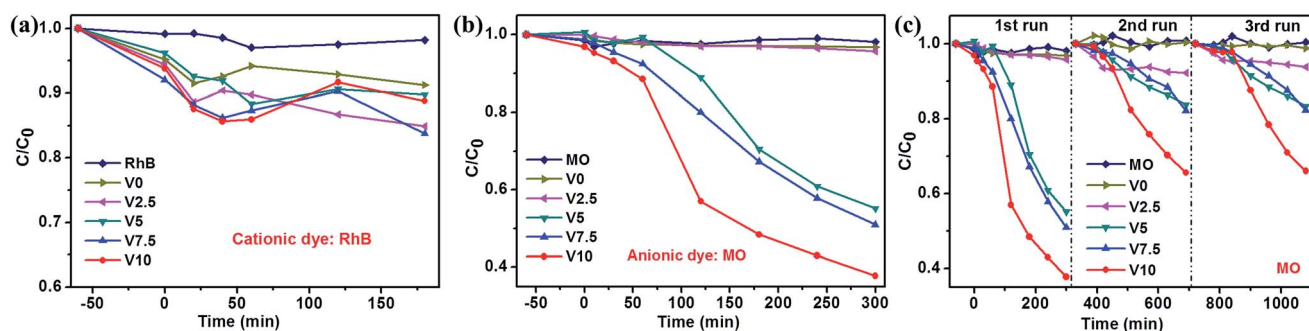

Fig. 4 Photodegradation of RhB (a) and MO (b) over as-prepared samples under visible light irradiation; (c) catalysts recycling in the photodegradation of MO.
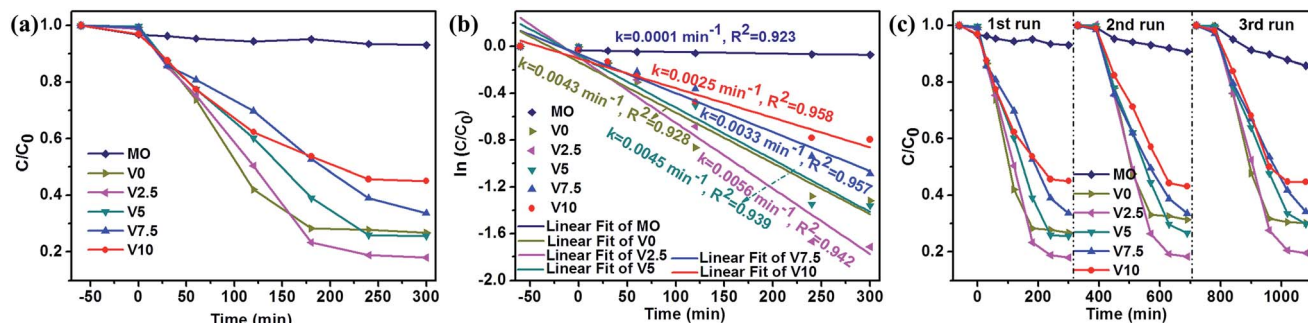
Fig. 5 Photocatalytic degradation of MO in the presence of H_2O_2 under visible light irradiation: (a) the overall analysis for all the products, (b) first-order kinetic plot of $\ln(C/C_0)$ *vs.* time, and (c) cycling test of all photocatalysts.

literatures:[6,18,29,57–64] (1) Cu_xO showing different adsorption ability to MO would affect the photocatalytic activity; (2) the exposed facets of as-prepared samples has an important effect on the photocatalytic performance;[51] (3) the formed heterojunction acting as a rapid separation site for the photogenerated electron–hole pairs promoted the photocatalytic efficiency; (4) H_2O_2 also had significant influence on the photocatalytic property. For the photodegradation process without H_2O_2, the photocatalytic reaction would be very simple: both CuO and Cu_2O could efficiently generate electrons and holes under visible light irradiation, then, the photogenerated electrons and holes reacted with H_2O and O_2 to generate oxidant species such as $\cdot OOH$, $\cdot OH$, and $\cdot O_2^-$.[26,46] Finally, the dyes (MO) could be effectively bleached by these oxidant species. The sequence of as-prepared samples for MO photodegradation without H_2O_2 could be explained that: (a) Cu_2O had the higher photocatalytic activity than CuO for MO degradation leading to the smallest photodegradation rate of V0, in well agreement with the literatures;[57–59] (b) the more amount of Cu_2O resulting in the increased photodegradation rate (V7.5 > V5 > V2.5), which was in consistent with XRD results and the previous report;[18] (c) {111} facets had the higher photocatalytic activity than that of other facets for Cu_2O, which was in accordance with SEM observation and confirmed by many other researches,[6,18,46,52,64] giving rise to the photodegradation rate of V10 > V7.5. Once H_2O_2 was added in the decoloration process, the mechanism became complicated. H_2O_2 was considered as an electron acceptor to promote the electron–hole separation and decompose to form a certain amount of $\cdot OH$ by accepting electrons to enhance the photocatalytic activity.[47,62] On the other hand, H_2O_2 could accelerate the photocorrosion of Cu_2O transforming into CuO which would lower the photocatalytic activity to some extent.[29,46,47] Therefore, the addition of H_2O_2 resulted in the relatively lower photodegradation rate of V7.5 and V10 due to the more severe photocorrosion compared with the photodegradation without H_2O_2. For V0 (pure CuO) the photodegradation rate had a faster increase due to the effect of H_2O_2, which was also found by other report.[62] Combining with H_2O_2, the photocatalytic activity of V2.5 and V5 was also stimulated to achieve a higher value. This might be caused by the interface between CuO and Cu_2O acting as a rapid separation site for the photogenerated electrons and holes and thus enhancing the photocatalytic performance.[59,62] Therefore, V2.5 had the highest

photodegradation rate due to the less photocorrosion induced by the relatively low content of Cu_2O and the protection from CuO.[6] In addition, the faster formation of CuO could protect the surface of Cu_2O resulting in the good durability of as-prepared samples under the photodegradation. Moreover, the specific surface area was considered to be very important factor for the photodegradation.[18,62] The specific surface areas of as-synthesized samples were evaluated to be 25.26, 19.44, 10.45, 6.20, and 6.66 $m^2\ g^{-1}$, for V0, V2.5, V5, V7.5, and V10, respectively (N_2 adsorption–desorption isotherms of the products were shown in ESI: Fig. SI-7†). Therefore, in our work, the specific surface area was not as important as other factors mentioned above.

In order to further understand the underlying photodegradation mechanism of as-synthesized samples, the structural and morphological studies were carried out for the typical samples V2.5 and V10. Fig. 6 presents the XRD patterns of V2.5 and V10 treated by different conditions. The patterns could be perfectly indexed with Cu_2O and CuO for V2.5 after photodegradation as shown in Fig. 6a, which confirmed that the composite was not changed by photodegradation. Only Cu_2O was observed for V10 before and after photodegradation as depicted in Fig. 6b. CuO could not be observed from XRD patterns in Fig. 6b, which was different from above assumption.

XPS analysis was used to examine the surface composition of the samples V2.5 and V10. Fig. 7 presents XPS spectra of V2.5 and V10 recorded by as-prepared samples and after MO photodegradation. The survey scan of V2.5 and V10 were observed as shown in Fig. 7a and d, which showed no obvious difference before and after photodegradation. As shown in Fig. 7b, high resolution XPS spectrum in the Cu $2p_{3/2}$ and Cu $2p_{1/2}$ binding energy region shows the major peaks locating at 933.8 and 954.5 eV are in consistent with the reported value of CuO, while the peaks located at 932.5 and 952.6 eV are assigned to Cu_2O.[18,64,65] The typical satellite peaks at 942 and 962.2 eV are also indexed to CuO[18,27,59,64,65] and the peaks showed slightly decrease after photodegradation illustrating the decrease of CuO content on the surface of sample V2.5. The O 1s region in Fig. 7c could be fit into three main peaks locating at 529.6, 530.2 and 531.3 eV, which are ascribed to the Cu–O bond of CuO, lattice oxygen of Cu_2O and surface-absorbed oxygen species (O_2 and H_2O), respectively.[43,65,66] All the XPS analysis confirms the existence of both CuO and Cu_2O in the sample V2.5 before and
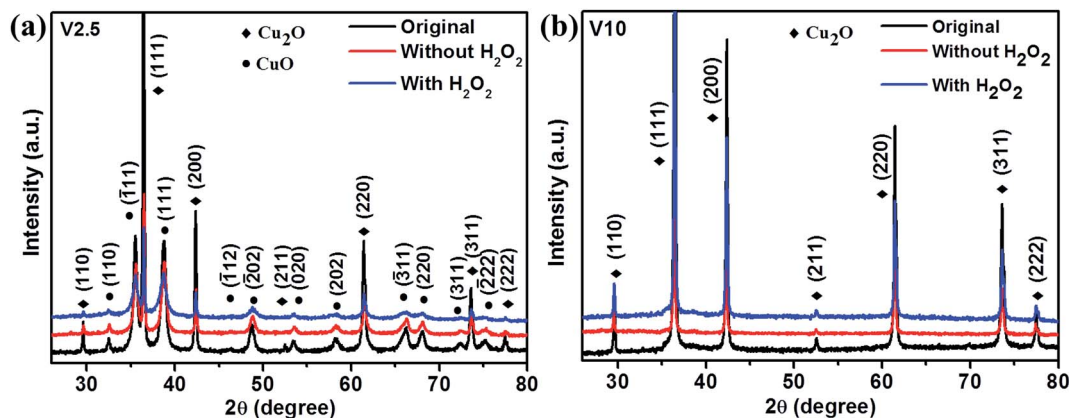
Fig. 6 XRD patterns of (a) V2.5 and (b) V10 before and after the photodegradation of MO with and without H_2O_2.
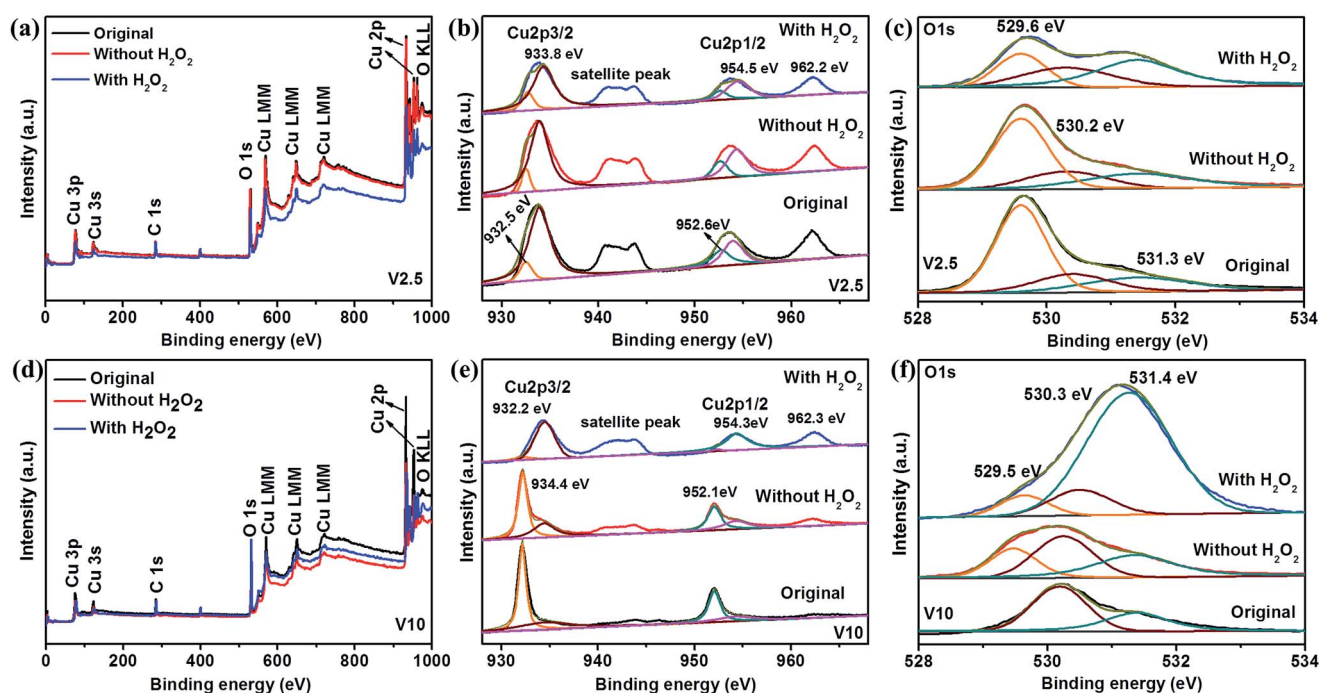

Fig. 7 Typical XPS analysis of V2.5 (upper panel) and V10 (lower panel) before and after photodegradation of MO with different conditions including XPS full spectrum, Cu 2p spectrum, and O 1s spectrum, respectively.

after photodegradation under different conditions, in agreement with XRD results. In addition, the intensities of O 1s at 529.6 eV and 531.3 eV become gradually lower and higher in the absence and presence of H_2O_2 for the degradation of MO, which demonstrates the decrease of CuO and increase of absorbed oxygen species on the surface of sample V2.5, respectively.[66,67] The decrease of CuO on the surface of sample V2.5 may be ascribed to reduce CuO to form Cu_2O by the photogenerated electrons,[68] which further explained by the junction formation resulted in the electron transfer direction.[6] However, the opposite results are observed in Fig. 7e and f due to the single phase of Cu_2O for as-prepared sample V10. The intensity of satellite peak in Cu 2p region becomes stronger after the photodegradation with H_2O_2 illustrating the more content of

surface CuO due to the more severe photocorrosion of Cu_2O.[29,47,67] In this case, the photocorrosion of Cu_2O is dominant compared with the CuO reduction, and thus CuO increases after photodegradation. Moreover, CuO observed in the sample V10 after photodegradation is different from XRD result which could be attributed to the trace amount of CuO on the surface of the samples.[65,66] Meanwhile, the intensity of O 1s at 531.4 eV becomes stronger under the photodegradation treatment with H_2O_2, demonstrating the bigger amount of surface-absorbed oxygen species.[67] The more adsorbed oxygen species would lead to the more generation of hydroxyl radical, which could effectively decolorize MO dye.[63] Therefore, it was reasonable for the enhanced photodegradation rate with H_2O_2 for all the samples.
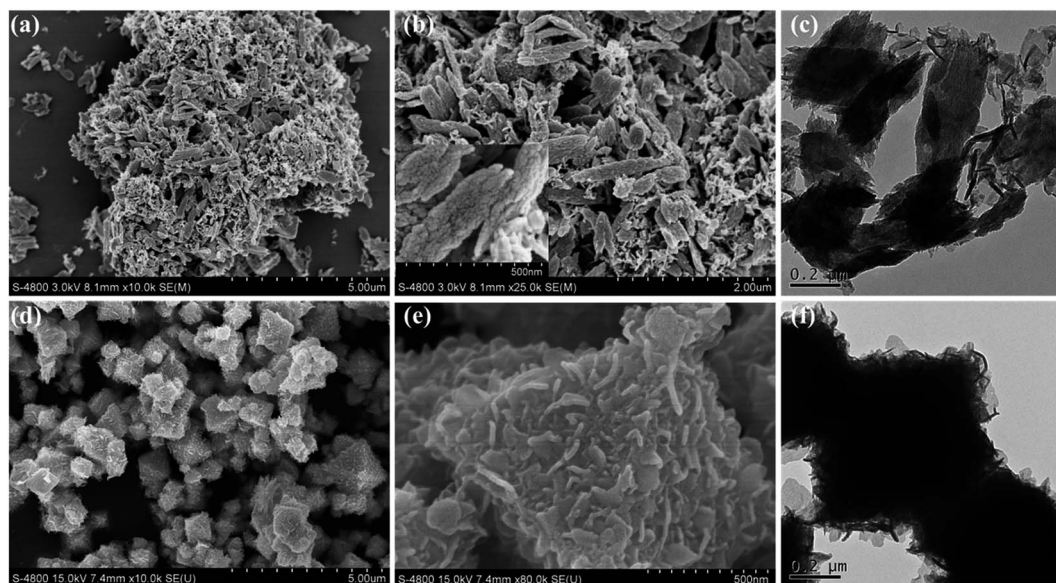
Fig. 8 SEM (a, b, d and e) and TEM (c and f) images of as-prepared sample V2.5 (upper panel) and V10 (lower panel) after photodegradation of MO in the presence of H_2O_2 under visible light irradiation. Inset of (b) is the magnified SEM images of original nanosheets.

The SEM and TEM observations were carried out to investigate the morphological change of as-prepared samples under photodegradation process. After photodegradation with H_2O_2, the nanosheets and flakes were observed for sample V2.5 as shown in Fig. 8a, which was different from the original structures (nanosheets and octahedron in Fig. 2b). Meanwhile, the octahedral structures for V10 (Fig. 8d) were observed which retained the original structures before photodegradation (Fig. 2f). However, from the magnified SEM images, the octahedrons were completely consisted of flakes (Fig. 8e) for V10. Meanwhile, the original nanosheets were full of pores (inset of Fig. 8b) as well as the incompact octahedrons (Fig. 2c) changed into disperse flakes during the photocatalytic process for V2.5. All the observations illustrated the morphology changes during the photocatalytic process, which was consistent with the previous reports.[18,63] Briefly, Cu_2O and CuO could experience mutual transformation due to the photocorrosion and reduction by the photogenerated electrons, respectively. The reaction occurred at the surface of catalysts, resulting in the following possible deduction. Some part of generated Cu_2O and CuO due to the photocatalysis could drop out from the surface of catalysts, leading to the final surface morphology transformation of photocatalysts. TEM images (Fig. 8c and f) further confirmed that the octahedrons were composed of flakes for V10 while sample V2.5 possessed porous nanosheets and disperse flakes. The results further deduced that the photocatalytic reaction occurred on the surface of as-prepared samples.

4.   Conclusions

In summary, Cu_xO (CuO, CuO/Cu_2O composite, and Cu_2O) nanostructures were successfully synthesized by a facile solution method under low temperature. The structural and morphological investigation proved that the amount of

hydroxylamine hydrochloride had played an important role in the composition and morphological transformation of as-grown samples. The photocatalytic activity study confirmed that as-synthesized samples presented the selectivity to the dyes under visible light irradiation and H_2O_2 significantly enhanced the photodegradation rate for MO in aqueous solution. The following factors should be considered for the possible mechanism on the photodegradation of organic dyes: the adsorption ability of photocatalysts, the structural and morphological character of as-prepared samples, the composition of photocatalysts, and the addition of H_2O_2. The post-photodegradation analysis illustrated that (1) as-prepared samples were stable; (2) the existence of CuO could inhibit the photocorrosion of Cu_2O; (3) the photocatalytic reaction occurred on the surface of photocatalysts. The results illustrated the potential application of Cu_xO in wastewater treatment and could be very important on the selection and design of metal oxide catalysts.

Acknowledgements

References

1 E. Eltzov, V. Pavluchkov, M. Burstin and R. S. Marks, *Sens. Actuators, B*, 2011, **155**, 859–867.
2 L. J. Zhou, Y. C. Zou, J. Zhao, P. P. Wang, L. L. Feng, L. W. Sun, D. J. Wang and G. D. Li, *Sens. Actuators, B*, 2013, **188**, 533–539.

3 B. Kumar, S. Saha, A. Ganguly and A. K. Ganguli, *RSC Adv.*, 2014, **4**, 12043–12049.

4 P. Basnet, G. K. Larsen, R. P. Jadeja, Y.-C. Hung and Y. P. Zhao, *ACS Appl. Mater. Interfaces*, 2013, **5**, 2085–2095.

5 L. L. Ma, J. L. Li, H. Z. Sun, M. Q. Qiu, J. B. Wang, J. Y. Chen and Y. Yu, *Mater. Res. Bull.*, 2010, **45**, 961–968.

6 P. Basnet and Y. P. Zhao, *Catal. Sci. Technol.*, 2016, **6**, 2228–2238.

7 A. Kudo and Y. Miseki, *Chem. Soc. Rev.*, 2009, **38**, 253–278.

8 L. L. Wang, J. Ge, A. L. Wang, M. S. Deng, X. J. Wang, S. Bai, R. Li, J. Jiang, Q. Zhang, Y. Luo and Y. J. Xiong, *Angew. Chem., Int. Ed.*, 2014, **53**, 5107–5111.

9 X. Wan, X. Y. Liang, C. R. Zhang, X. X. Li, W. W. Liang, H. S. Xu, S. Lan and S. L. Tie, *Chem. Eng. J.*, 2015, **272**, 58–68.

10 X. Xu, Z. H. Gao, Z. D. Cui, Y. Q. Liang, Z. Y. Li, S. L. Zhu, X. J. Yang and J. M. Ma, *ACS Appl. Mater. Interfaces*, 2016, **8**, 91–101.

11 G. Mamba and A. K. Mishra, *Appl. Catal., B*, 2016, **198**, 347–377.

12 F. Dong, Z. W. Zhao, T. Xiong, Z. L. Ni, W. D. Zhang, Y. J. Sun and W.-K. Ho, *ACS Appl. Mater. Interfaces*, 2013, **5**, 11392–11401.

13 M. Manikandan, T. Tanabe, P. Li, S. Ueda, G. V. Ramesh, R. Kodiyath, J. J. Wang, T. Hara, A. Dakshanamoorthy, S. Ishihara, K. Ariga, J. H. Ye, N. Umezawa and H. Abe, *ACS Appl. Mater. Interfaces*, 2014, **6**, 3790–3793.

14 W. Jiang, Z. M. Wu, X. N. Yue, S. J. Yuan, H. F. Lu and B. Liang, *RSC Adv.*, 2015, **5**, 24064–24071.

15 X. Zheng, Z. C. Han, S. Y. Yao, H. H. Xiao, F. Chai, F. Y. Qu and X. Wu, *Dalton Trans.*, 2016, 7094–7103.

16 S. S. Dunkle, R. J. Helmich and K. S. Suslick, *J. Phys. Chem. C*, 2009, **113**, 11980–11983.

17 X. Wang, J. Yang, L. X. Shi and M. Z. Gao, *Nanoscale Res. Lett.*, 2016, **11**, 125.

18 M. A. Nguyen, N. M. Bedford, Y. Ren, E. M. Zahran, R. C. Goodin, F. F. Chagani, L. G. Bachas and M. R. Knecht, *ACS Appl. Mater. Interfaces*, 2015, **7**, 13238–13250.

19 J. C. Park, J. H. Kim, H. S. Kwon and H. J. Song, *Adv. Mater.*, 2009, **21**, 803–807.

20 H. M. Wei, H. B. Gong, L. Chen, M. Zi and B. Q. Cao, *J. Phys. Chem. C*, 2012, **116**, 10510–10515.

21 L. Hu, Y. M. Huang, F. P. Zhang and Q. W. Chen, *Nanoscale*, 2013, **5**, 4186–4190.

22 P. P. Xu, J. J. Liu, T. Liu, K. Ye, K. Cheng, J. L. Yin, D. X. Cao, G. L. Wang and Q. Li, *RSC Adv.*, 2016, **6**, 28270–28278.

23 D. S. Murali, S. Kumar, R. J. Choudhary, A. D. Wadikar, M. K. Jain and A. Subrahmanyam, *AIP Adv.*, 2015, **5**, 047143.

24 M. Hara, T. Kondo, M. Komoda, S. Ikeda, K. Shinohara, A. Tanaka, J. N. Kondo and K. Domen, *Chem. Commun.*, 1998, **3**, 357–358.

25 H. Xu, W. Wang and W. Zhu, *J. Phys. Chem. B*, 2006, **110**, 13829–13834.

26 J. Shi, J. Li, X. J. Huang and Y. W. Tan, *Nano Res.*, 2011, **4**, 448–459.

27 C. S. Dong, M. L. Zhong, T. Huang, M. X. Ma, D. Wortmann, M. Brajdic and I. Kelbassa, *ACS Appl. Mater. Interfaces*, 2011, **3**, 4332–4338.

28 Y. Yu, L. Y. Zhang, J. Wang, Z. Yang, M. C. Long, N. T. Hu and Y. F. Zhang, *Nanoscale Res. Lett.*, 2012, **7**, 347.

29 W. Zhai, F. Q. Sun, W. Chen, L. H. Zhang, Z. L. Min and W. S. Li, *Mater. Res. Bull.*, 2013, **48**, 4953–4959.

30 L. Liu, Y. H. Qi, J. S. Hu, Y. H. Liang and W. Q. Cui, *Appl. Surf. Sci.*, 2015, **351**, 1146–1154.

31 J. T. Zhang, J. F. Liu, Q. Peng, X. Wang and Y. D. Li, *Chem. Mater.*, 2006, **18**, 867–871.

32 Z. J. Li, N. N. Wang, Z. J. Lin, J. Q. Wang, W. Liu, K. Sun, Y. Q. Fu and Z. G. Wang, *ACS Appl. Mater. Interfaces*, 2016, **8**, 20962–20968.

33 K. B. Zhou, R. P. Wang, B. Q. Xu and Y. D. Li, *Nanotechnology*, 2006, **17**, 3939–3943.

34 B. Pecquenard, F. L. Cras, D. Poinot, O. Sicardy and J.-P. Manaud, *ACS Appl. Mater. Interfaces*, 2014, **6**, 3413–3420.

35 D. P. Dubal, G. S. Gund, R. Holze, H. S. Jadhav, C. D. Lokhandeb and C.-J. Park, *Dalton Trans.*, 2013, **42**, 6459–6467.

36 G. A. Artioli, A. Mancini, V. R. Barbieri, M. C. Quattrini, E. Quartarone, M. C. Mozzati, G. Drera, L. Sangaletti, V. Gombac, P. Fornasiero and L. Malavasi, *Langmuir*, 2016, **32**, 1510–1520.

37 S. Zaman, A. Zainelabdin, G. Amin, O. Nur and M. Willander, *J. Phys. Chem. Solids*, 2012, **73**, 1320–1325.

38 L. J. Wang, Q. Zhou, Y. J. Liang, H. L. Shi, G. L. Zhang, B. S. Wang, W. W. Zhang, B. Lei and W. Z. Wang, *Appl. Surf. Sci.*, 2013, **271**, 136–140.

39 L. J. Wang, Q. Zhou, G. L. Zhang, Y. J. Liang, B. S. Wang, W. W. Zhang, B. Lei and W. Z. Wang, *Mater. Lett.*, 2012, **74**, 217–219.

40 M. Yurddaskal, T. Dikici and E. Celik, *Ceram. Int.*, 2016, **42**, 17749–17753.

41 M. Villani, A. B. Alabi, N. Coppedè, D. Calestani, L. Lazzarini and A. Zappettini, *Cryst. Res. Technol.*, 2014, **49**, 594–598.

42 V. Scuderi, G. Amiard, S. Boninelli, S. Scalese, M. Miritello, P. M. Sberna, G. Impellizzeri and V. Privitera, *Mater. Sci. Semicond. Process.*, 2016, **42**, 89–93.

43 F. Wu, S. Banerjee, H. F. Li, Y. Myung and P. Banerjee, *Langmuir*, 2016, **32**, 4485–4493.

44 Y. Y. Duan, X. Liu, L. Han, S. Asahina, D. D. Xu, Y. Y. Cao, Y. Yao and S. A. Che, *J. Am. Chem. Soc.*, 2014, **136**, 7193–7196.

45 M. Vaseem, A. Umar, S. H. Kim and Y.-B. Hahn, *J. Phys. Chem. C*, 2008, **112**, 5729–5735.

46 X. L. Deng, Q. Zhang, Q. Q. Zhao, L. S. Ma, M. Ding and X. J. Xu, *Nanoscale Res. Lett.*, 2015, **10**, 8.

47 G. D. Wu, W. Zhai, F. Q. Sun, W. Chen, Z. Z. Pan and W. S. Li, *Mater. Res. Bull.*, 2012, **47**, 4026–4030.

48 K. Govender, D. S. Boyle, P. B. Kenway and P. O'Brien, *J. Mater. Chem.*, 2004, **14**, 2575–2591.

49 S.-O. Kang, S. H. Hong, J. S. Choi, J.-S. Kim, I. R. Hwang, I.-S. Byun, Y. S. Kim, W. D. Kim and B. H. Park, *J. Appl. Phys.*, 2010, **107**, 053704.

50 H. H. Wang, C. S. Xie, D. W. Zeng and Z. H. Yang, *J. Colloid Interface Sci.*, 2006, **297**, 570–577.

51 C.-H. Kuo and M. H. Huang, *J. Phys. Chem. C*, 2008, **112**, 18355–18360.

52 J.-Y. Ho and M. H. Huang, *J. Phys. Chem. C*, 2009, **113**, 14159–14164.

53 C.-H. Kuo, T.-E. Hua and M. H. Huang, *J. Am. Chem. Soc.*, 2009, **131**, 17871–17878.

54 B. High, D. Bruce and M. M. Richter, *Anal. Chim. Acta*, 2001, **449**, 17–22.

55 P. S. Rendell, G. E. Batley and A. J. Cameron, *Environ. Sci. Technol.*, 1980, **14**, 314–318.

56 C. L. Allen, B. N. Atkinson and J. M. J. Williams, *Angew. Chem., Int. Ed.*, 2012, **51**, 1383–1386.

57 J. L. Liu, Z. Y. Gao, H. J. Han, D. P. Wu, F. Xu, H. X. Wang and K. Jiang, *Chem. Eng. J.*, 2012, **185–186**, 151–159.

58 C. H. Wang, Y. X. Ye, B. Tao and B. Y. Geng, *CrystEngComm*, 2012, **14**, 3677–3683.

59 R. C. Yang, Z. H. Zhang, Y. M. Ren, X. Zhang, Z. M. Chen and M. D. Xu, *Mater. Sci. Technol.*, 2015, **31**, 25–30.

60 L. Huang, F. Peng, H. Yu and H. J. Wang, *Solid State Sci.*, 2009, **11**, 129–138.

61 Y. Bessekhouad, D. Robert and J. V. Weber, *Catal. Today*, 2005, **101**, 315–321.

62 H. G. Yu, J. G. Yu, S. W. Liu and S. Mann, *Chem. Mater.*, 2007, **19**, 4327–4334.

63 Z. K. Zheng, B. B. Huang, Z. Y. Wang, M. Guo, X. Y. Qin, X. Y. Zhang, P. Wang and Y. Dai, *J. Phys. Chem. C*, 2009, **113**, 14448–14453.

64 L. H. Zhang and X. F. Wang, *Appl. Phys. A*, 2014, **117**, 2189–2196.

65 X. F. Lin, R. M. Zhou, J. Q. Zhang and S. T. Fei, *Appl. Surf. Sci.*, 2009, **256**, 889–893.

66 X. L. Deng, Q. Zhang, E. Zhou, C. J. Ji, J. Z. Huang, M. H. Shao, M. Ding and X. J. Xu, *J. Alloys Compd.*, 2015, **649**, 1124–1129.

67 Y. L. Du, N. Zhang and C. M. Wang, *Catal. Commun.*, 2010, **11**, 670–674.

68 J. Bandara, I. Guasaquillo, P. Bowen, L. Soare, W. F. Jardim and J. Kiwi, *Langmuir*, 2005, **21**, 8554–8559.